Contents

Part I

Measurement of the jet transverse-momentum resolution

1 Introduction

The determination and quantification of the quality of the jet transverse-momentum measurement is of crucial interest for many analyses with jet final states, e. g. the measurement of the dijet cross section [1] or $t\bar{t}$ production cross sections [2]. Also searches for physics beyond the standard model with missing transverse momentum, $\not{p}_\mathrm{T}$, in the final state need a good knowledge of $\not{p}_\mathrm{T}$ originating from wrongly measured jets [3–5]. For analyses relying on information from simulation it is very important to correct the simulated resolution to the resolution actually present in data. Therefore, scale factors will be presented to adjust the resolution in simulation to the resolution of the real detector.

In the following sections, a data-based method to measure the jet p_T resolution in $\gamma + \mathrm{jet}$ events will be presented. A similar method was already accomplished in earlier analyses [6, 7] of 7 TeV data. It is further developed here and applied to $19.7\,\mathrm{fb}^{-1}$ of $\sqrt{s} = 8\,\mathrm{TeV}$ data.

The method is based on the transverse-momentum balance in the $\gamma + \mathrm{jet}$ system. It takes advantage of the high resolution of the electromagnetic calorimeter and hence the excellent measurement of the photon energy and momentum. Without initial and final state radiation, the photon and the jet are balanced in the transverse plane. Thus, measuring the photon p_T with high accuracy leads to an estimate of the true jet transverse momentum offering a possibility to quantify the resolution of jet p_T measurements.

2 General approach of the resolution measurement using photon+jet events

The jet transverse-momentum resolution is defined as the standard deviation of the jet transverse-momentum response distribution with the response defined as the ratio of the reconstructed to the generator-level jet transverse momentum

$$\mathcal{R} = \frac{p_\mathrm{T}^{\mathrm{reco.\,jet}}}{p_\mathrm{T}^{\mathrm{gen.\,jet}}}. \tag{2.1}$$

For each reconstructed jet, the underlying generator-level jet is hereby found by matching the closest generator-level jet to the reconstructed jet with $\Delta R = \sqrt{(\Delta\phi)^2 + (\Delta\eta)^2}$ with a maximal value of $\Delta R_{\mathrm{max}} = 0.25$. Furthermore, the transverse momentum of the generator-level jet is defined as the sum of all particles' transverse momenta from the hadronisation that are clustered into the jet cone. Throughout the following sections, the jet transverse-momentum resolution will be abbreviated JER[1]. The mean of the response distribution will be referred to as jet energy scale (JES).

Figure 2.1 shows a response distribution for jets in the barrel region. The core of the response distribution shows the typical Gaussian behaviour whereas the tails deviate from that functional form. Physical reasons for the low response tail are inter alia semi-leptonic decays of heavy quarks where the neutrino cannot be detected and the reconstructed transverse momentum of the jet is too small. This effect is visible in Fig. 2.1 because the neutrinos are included into the generator-level jet. Some instrumental effects, such as a non-linear response of the calorimeter, inhomogeneities of the detector material and electronic noise can contribute to both tails, others, like dead calorimeter channels only contribute to the left tail. The resolution is therefore determined using only the core of the distribution to avoid the coverage of non-Gaussian tails. The resolution is thus defined as the standard deviation of the 99% truncated response histogram divided by the mean of the histogram:
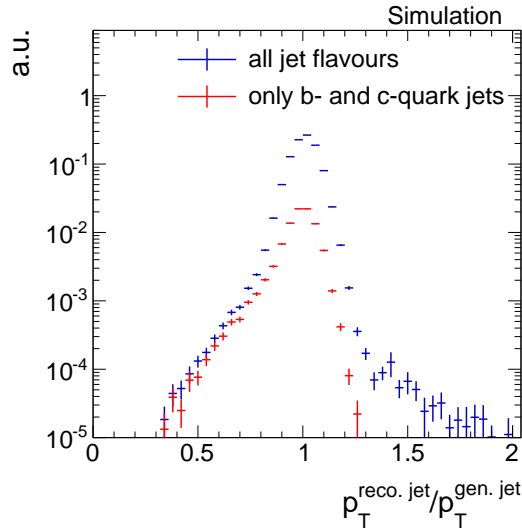
Figure 2.1: Normalised number of events over $p_{\mathrm{T}}^{\mathrm{reco.\,jet}}/p_{\mathrm{T}}^{\mathrm{gen.\,jet}}$ from a simulated $\gamma + \mathrm{jet}$ sample. The contribution by c- and b-quark jets is shown in red, which cause almost fully the left tail originating from semi-leptonic decays.

---

[1]This abbreviation is a historical relic from experiments where the momentum of jets were only measured in the calorimeters and therefore JER referred to jet energy resolution.

$$\sigma_{\mathrm{JER}} = \frac{\sigma_{99\%}}{\mu_{99\%}}.$$

The determination of the 99% range of the histogram is done in several steps. First the mean of the core is found via a Gaussian fit to the histogram in a 2σ range[2]. This procedure is done in three iteration steps. Then, a symmetric interval around this mean is determined with its integral equal to 99% of the integral of the full histogram. The division by the mean aims to make the resolution independent of the absolute scale (= mean) of the response distribution. It is done because response distributions with a scale smaller than one are typically narrower while distributions with scales larger than one are broader. However, since after the application of the jet energy corrections the scale is very close to one, this is only a tiny effect.

The evaluation of the response distribution as reconstructed over generator-level jet transverse momentum (Eq. (2.1)) is only possible for simulated events where generator-level information is accessible. A determination of the resolution in data, however, has to rely on a different approach.

The main idea of a resolution measurement using γ+jet events is based on the transverse-momentum balance of the γ + jet system and the excellent electromagnetic calorimeter resolution (which was estimated between 1.4% and 3.8% in the barrel region for photons for $\sqrt{s} = 8\,\mathrm{TeV}$ data [8]).

In Fig 2.2, all tree-level processes contributing to an event topology with one photon and one jet in the final state are depicted. Due to momentum conversation, the jet and the photon are back to back in the transverse plane, and therefore, $\vec{p}^{\,\gamma} = -\vec{p}^{\,\mathrm{jet}}$. Because of the good resolution of the electromagnetic calorimeter, photon momenta can be very well measured and thus can serve as an excellent estimator for the true jet momentum.

Unfortunately, such clean events are very rare processes, and usually, the momentum balance is spoiled by initial and final state radiation, which lead to further jets in the event (see Fig. 2.3). However, in order to select events that are balanced to a large extent, a lower bound on the angular distance in the transverse plane between the photon and the jet
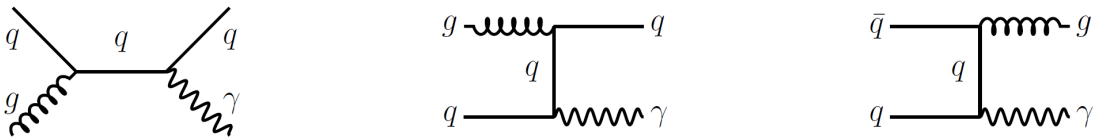

Figure 2.2: Tree-level Feynman diagrams of processes at the LHC in *pp*-collisions with one photon and one jet in the final state.

---

[2]The 2σ range is defined as the range $[\mu - 2\sigma, \mu + 2\sigma]$.

Figure 2.3: Tree-level Feynman diagrams with initial and final state radiation.

with the highest transverse momentum (leading jet) is required: $\Delta\Phi\left(1^{\text{st}}\,\text{jet}, \gamma\right) > 2.95\,\text{rad}$.

Additionally, the variable

$$\alpha \doteq \frac{p_{\text{T}}^{2^{\text{nd}}\,\text{reco.\,jet}}}{p_{\text{T}}^{\gamma}}$$

is defined as a measure of further jet activity in an event. It is, however, not sufficient to require only an upper bound on α. Instead, the jet transverse-momentum resolution is measured in bins of α (with $\max(\alpha) = 0.2$), and the extrapolated value to zero further jet p_{T} ($\alpha = 0$) is taken as the measured resolution of the jet p_{T} in the absence of further jets.

Measuring the transverse momentum of the photon instead of taking the generator-level jet p_{T} leads to the fact that the measured resolution consists out of two parts

$$\frac{p_{\text{T}}^{\text{reco.\,jet}}}{p_{\text{T}}^{\gamma}} = \underbrace{\frac{p_{\text{T}}^{\text{reco.\,jet}}}{p_{\text{T}}^{\text{gen.\,jet}}}}_{\text{intrinsic}} \cdot \underbrace{\frac{p_{\text{T}}^{\text{gen.\,jet}}}{p_{\text{T}}^{\gamma}}}_{\text{imbalance}} \; .$$

The intrinsic part is the resolution of interest which is independent of further jets in the event whereas the imbalance is strongly dependent on α.

To extract the intrinsic resolution out of the measured one, the residual imbalance q (the imbalance at $\alpha = 0$) is subtracted from the total resolution in the limit of vanishing additional jet activity. Since this information is only available from simulation, the measured resolution in data is corrected by the residual imbalance taken from the simulated dataset.

To account for differences in the jet transverse-momentum resolution for different true jet p_{T} and different jet pseudorapidity regions, the measurement of the resolution is done in p_{T}^{γ} bins and bins of $|\eta|$ of the leading jet.

3 Datasets and event selection

The measurement of the jet transverse-momentum resolution is carried out with $\gamma + \text{jet}$ data recorded during the year 2012 at a centre-of-mass energy of $\sqrt{s} = 8\,\text{TeV}$ at the CMS experiment. The datasets and triggers that are exploited for this measurement are introduced in the following Section 3.1. The measured resolution in data is compared to the resolution in simulated samples. These are introduced in Section 3.2. In order to select $\gamma + \text{jet}$ events that are well suited for the resolution measurement, an event selection is applied on top. This event selection is described in Section 3.3.

3.1 Datasets and triggers

This analysis exploits several triggers which were active during the year 2012 at the CMS experiment. Because of the high production cross section of $\gamma + \text{jet}$ events, especially for low photon p_{T}, almost all of these triggers were highly prescaled, i. e. only a fraction of events were actually recorded when the triggers fired. All triggers that are utilised in this measurement are listed in Table 3.1 together with their recorded luminosity. The triggers rely on level one (L1) on single-photon triggers, such as L1SingleEG12 and L1SingleEG30.

Table 3.1: Single-photon triggers together with the recorded luminosity taking the prescales of the triggers into consideration.

Trigger	Luminosity $[\,\text{fb}^{-1}\,]$
HLT_Photon30_CaloIdVL_IsoL	0.0029
HLT_Photon50_CaloIdVL_IsoL	0.0607
HLT_Photon75_CaloIdVL_IsoL	0.123
HLT_Photon90_CaloIdVL_IsoL	0.373
HLT_Photon135	13.77
HLT_Photon150	19.71

The L1 triggers require at least one photon that is above a certain p_T threshold, e. g. 12 GeV or 30 GeV. The high-level triggers require a photon with a certain p_T (as indicated in the name) and, in case of thresholds below 135 GeV also additional quality and isolation criteria. All triggers with threshold below 150 GeV were prescaled.

The events that are selected by the above mentioned triggers are contained in the datasets listed in Table 3.2.

Table 3.2: Single-photon data samples used for the resolution measurement with the contained integrated luminosity.

Dataset	Luminosity [fb^{-1}]
/Photon/Run2012A-22Jan2013-v1/AOD	0.876
/SinglePhoton/Run2012B-22Jan2013-v1/AOD	4.412
/SinglePhoton/Run2012C-22Jan2013-v1/AOD	7.055
/SinglePhotonParked/Run2012D-22Jan2013-v1/AOD	7.354

3.2 Simulated samples

In order to compare the measured resolution in data to the resolution in simulation, a single-photon sample simulated with PYTHIA6 is used. This sample is generated flat in the photon p_T to have a good statistical precision also for the high photon p_T region. In order to recover a physical p_T spectrum, all simulated events are reweighted. Figure 3.1 shows the photon p_T spectrum in simulation before and after the reweighting.

All simulated samples come with a pileup scenario which does not necessarily match the pileup scenario in data. To match the measured distribution of primary vertices, the events are weighted according to their number of primary vertices. Because almost all of the used triggers are differently prescaled, the distributions of primary vertices differ among the various events triggered by the corresponding trigger. Thus the reweighting has to be done separately for the events falling in the photon p_T range of the several triggers (see Table 3.3). A comparison between the number of primary vertices can be found in Appendix A.1 for all triggers.
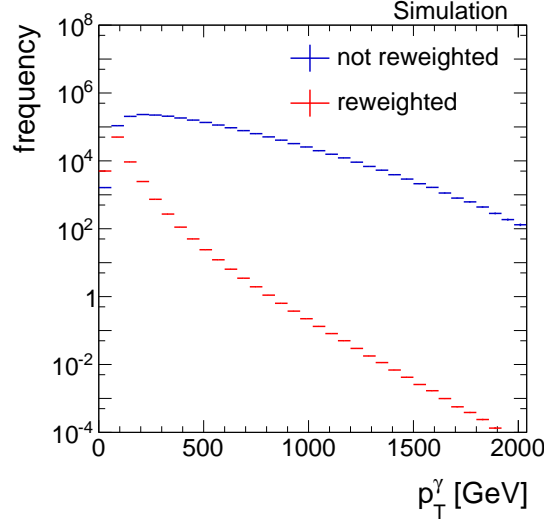
Figure 3.1: The photon p_T spectrum before (blue) and after (red) reweighting.

3.3 Event selection

Events are reconstructed with the particle-flow reconstruction algorithm, which uses information of all detector components to reconstruct individual particles [9]. In the following, the selection of well reconstructed jets and photons will be explained as well as the event selection of $\gamma +$ jet events.

3.3.1 Jet selection

Particles belonging to a jet are clustered with the Anti-k_t jet clustering algorithm with a radius of R=0.5 [10]. Furthermore, all reconstructed jets undergo a so-called "charged hadron subtraction" (CHS) which removes hadrons that are likely caused by pileup events.

To select clean $\gamma +$ jet events, it is required that the leading jet meets the following requirements (these criteria correspond to a 'tight ID' in [11, 12]):

- Neutral hadron fraction < 0.90

- Neutral electromagnetic fraction < 0.90

- Number of constituents > 1

And for jets in the pseudorapidity range $|\eta| < 2.4$:

- Charged hadron fraction > 0

- Charged hadron multiplicity > 0

- Charged electromagnetic fraction < 0.99

These selection cuts ensure a selection efficiency of around 99% and a noise rejection efficiency of 99.98% [11]. To mitigate effects from pileup, the first and second jet are required to have a transverse momentum greater $10\,\mathrm{GeV}$.

3.3.2 Photon selection

Concerning the photon, a maximal pseudorapidity of the photon of $|\eta^\gamma| < 1.3$ is demanded to exploit the high resolution of the ECAL in the barrel region.

Furthermore, the resolution is determined for different ranges in photon p_T to avoid mixing of different prescales of the various triggers. In Table 3.3 the applied binning is shown with the respective triggers contributing to each p_T^γ bin.

Table 3.3: Photon p_T bins and corresponding triggers.

p_T^γ-bins	Trigger
36 GeV	HLT_Photon30_CaloIdVL_IsoL_v*
60 GeV	HLT_Photon50_CaloIdVL_IsoL_v*
88 GeV	HLT_Photon75_CaloIdVL_IsoL_v*
105 GeV	HLT_Photon90_CaloIdVL_IsoL_v*
149 GeV	HLT_Photon135_v*
165 GeV	HLT_Photon150_v*

QCD-multijet events constitute an important background to the γ+jet events: A photon can be faked by a π^0 decaying into two close-by photons. Therefore, a very clean selection of the photons is necessary to suppress this background. The following variables are used (see [13] for further explanation of the variables):

- $\frac{\mathbf{H}}{\mathbf{E}}$: The ratio of the measured energy in the hadronic calorimeter over the energy measured in the electromagnetic calorimeter. For photons, this is supposed to be very small as they deposit their energy predominantly in the ECAL.

- $\boldsymbol{\sigma_{i\eta i\eta}}$: The energy weighted spatial width of the photon energy deposition. The electromagnetic shower of a photon has a small lateral size resulting in small $\sigma_{i\eta i\eta}$ for prompt photons while showers from fake photons, e.g. $\pi^0 \rightarrow \gamma\gamma$ have a larger lateral size.

- **Jurassic ECAL isolation**: This isolation criterion uses the information of reconstructed hits "RecHits" (coming from the local reconstruction of the digital signals) in a cone around the photon supercluster of R=0.4. Those are summed up and an upper criterion is identified to discriminate against background which is typically spatially broader.

- **Tower-based HCAL isolation**: The isolation criterion requires the energy deposited in all HCAL towers around the photon in cone of R=0.4 to be small compared to the photon's energy.

- **Hollow cone track isolation**: Requires absence of high-energetic tracks around the photon.

- **Pixel seed veto**: In order to reduce the background from electrons and positrons, the absence of a pixel-seed in the pixel tracker along the photons trajectory is required.

The upper and lower bounds that are set on these observables can be found in Table 3.4.

Table 3.4: Upper and lower bounds for all photon isolation criteria in the barrel $(|\eta^\gamma| < 1.4442)$.

	Barrel
$\frac{\text{H}}{\text{E}}$	< 0.05
$\sigma_{i\eta i\eta}$	< 0.013
ECAL isolation	$< 4.2\,\text{GeV} + 0.0060 \cdot p_\text{T}^\gamma$
HCAL isolation	$< 2.2\,\text{GeV} + 0.0025 \cdot p_\text{T}^\gamma$
Track Isolation	$< 2.0\,\text{GeV} + 0.0010 \cdot p_\text{T}^\gamma$
Pixel seed veto	yes

3.3.3 Photon+jet event selection

Besides the mentioned requirements concerning the objects' attributes, two further criteria related to the event topology are crucial for this analysis:

An upper threshold on $\Delta\Phi$ between the leading jet and the photon and a maximal value for α

- $\Delta\Phi\left(1^{\text{st}}\,\text{jet},\,\gamma\right) > 2.95\,\text{rad}$

- $\frac{p_{\text{T}}^{2^{\text{nd}}\,\text{jet}}}{p_{\text{T}}^{\gamma}} < 0.20.$

These requirements are important to suppress events with too much further hadronic activity.

A summary of all selection criteria can be found in Appendix A.2.

Finally, the leading jet pseudorapidity interval bounds need to be chosen in order to account for resolution differences in different detector regions. This is done according to [14] with the following binning

$$|\eta^{1^{\text{st}}\,\text{jet}}| = 0.0 - 0.5 \qquad\qquad |\eta^{1^{\text{st}}\,\text{jet}}| = 1.1 - 1.7$$
$$|\eta^{1^{\text{st}}\,\text{jet}}| = 0.5 - 1.1 \qquad\qquad |\eta^{1^{\text{st}}\,\text{jet}}| = 1.7 - 2.3.$$

The binning in the p_{T}^{γ} dimension is chosen according to the trigger thresholds for $p_{\text{T}}^{\gamma} < 165\,\text{GeV}$ and ensures sufficient statistical precision for $p_{\text{T}}^{\gamma} > 165\,\text{GeV}$

$$p_{\text{T}}^{\gamma} = 36 - 60\,\text{GeV} \qquad p_{\text{T}}^{\gamma} = 149 - 165\,\text{GeV} \qquad p_{\text{T}}^{\gamma} = 200 - 300\,\text{GeV}$$
$$p_{\text{T}}^{\gamma} = 60 - 88\,\text{GeV} \qquad p_{\text{T}}^{\gamma} = 165 - 176\,\text{GeV} \qquad p_{\text{T}}^{\gamma} = 300 - 400\,\text{GeV}$$
$$p_{\text{T}}^{\gamma} = 88 - 105\,\text{GeV} \qquad p_{\text{T}}^{\gamma} = 176 - 200\,\text{GeV} \qquad p_{\text{T}}^{\gamma} > 400\,\text{GeV}$$
$$p_{\text{T}}^{\gamma} = 105 - 149\,\text{GeV} \qquad p_{\text{T}}^{\gamma} = 300 - 400\,\text{GeV}.$$

4 Methodology of the measurement

The basic methodology of measuring the jet transverse-momentum resolution by exploiting the p_{T} balance in $\gamma + \text{jet}$ events and extrapolating the result to small α, that was already used in earlier analyses [6, 7], is extended in this measurement in order to explicitly distinguish the case of parton radiation in different event hemispheres.

As already described in Chapter 2, the idea behind a resolution measurement with $\gamma+\text{jet}$ events is the usage of the photon p_{T} instead of the true jet p_{T}. This results in a twofold contribution to the measured response, the intrinsic response and the imbalance:

$$\frac{p_{\mathrm{T}}^{\text{reco. jet}}}{p_{\mathrm{T}}^{\gamma}} = \underbrace{\frac{p_{\mathrm{T}}^{\text{reco. jet}}}{p_{\mathrm{T}}^{\text{gen. jet}}}}_{\text{intrinsic}} \cdot \underbrace{\frac{p_{\mathrm{T}}^{\text{gen. jet}}}{p_{\mathrm{T}}^{\gamma}}}_{\text{imbalance}} \; . \tag{4.1}$$

Taking the photon p_{T} as true jet p_{T} estimator instead of the generator jet p_{T}, and thus measuring the response defined as $p_{\mathrm{T}}^{\text{reco. jet}}/p_{\mathrm{T}}^{\gamma}$, results in a different shape of the response function as shown in Fig. 4.1. The figure compares the intrinsic response, the imbalance, and the measured total response in simulation.

The clear difference between the intrinsic response and the imbalance is the double peak structure of the latter one. The measured response is a convolution of the two
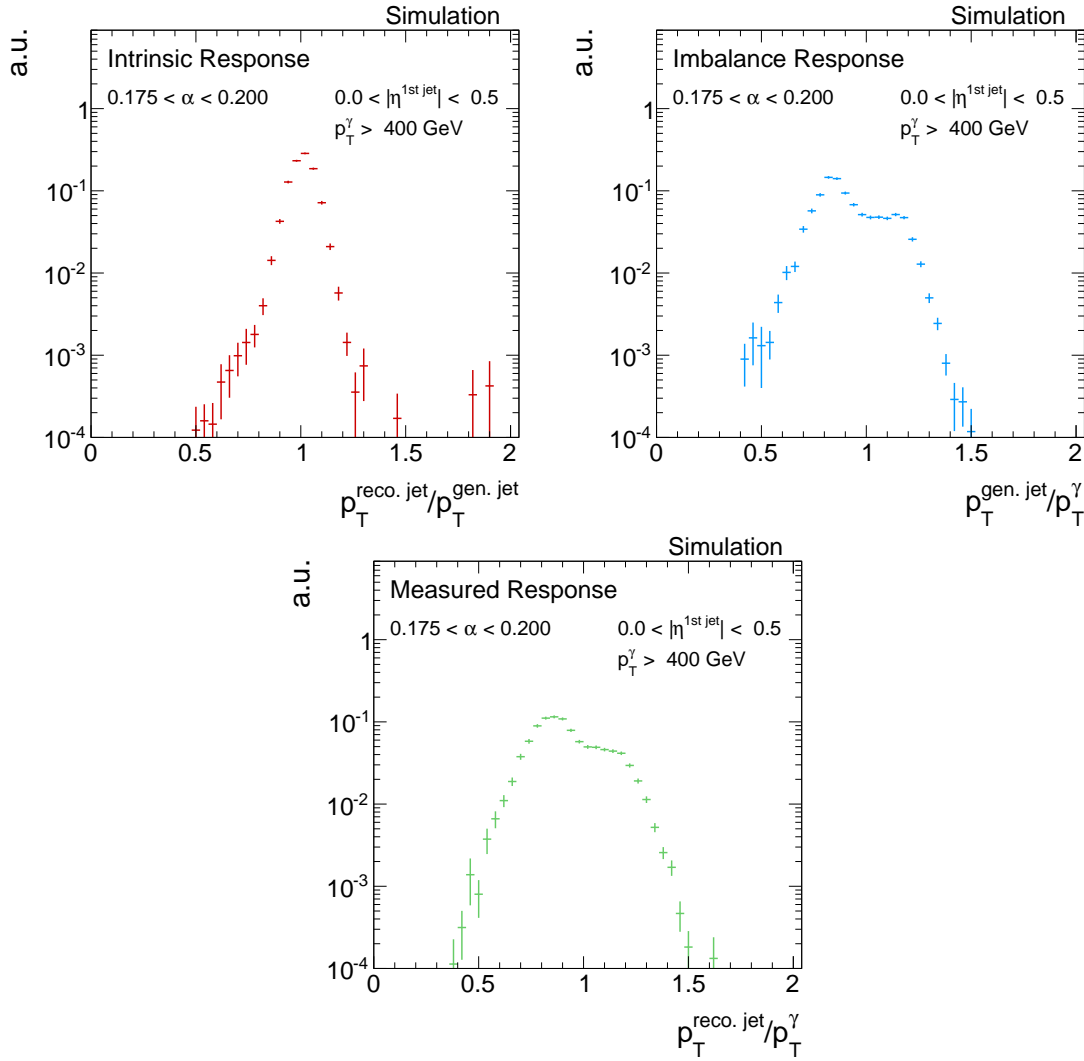

Figure 4.1: The two different contributions, intrinsic (top left) and imbalance (top right), to the measured response (bottom) (cf. Eq. (4.1)) in simulated events.

contributions, where the double peak is consequentially less pronounced.

The occurrence of two peaks is caused by the hard selection in $\Delta\phi$ which forces the second jet to be either close to the photon or close to the leading jet due to p_T conservation. The possibility of an energetic second jet perpendicular to the leading jet-photon axis which is balanced by a third jet is very unlikely due to the decreasing jet multiplicity in QCD-multijet events. The double peak structure is less pronounced for small second jet p_T (small α) where the $\Delta\Phi$ requirement does not have such a strong effect in rejecting events with a second jet perpendicular to the photon leading jet axis (see Fig. 4.2).

These two different contributions (second jet in photon/leading jet hemisphere) result in two separate response distribution. A schematic sketch of the two contributions is shown in Fig. 4.3.

The mathematical definitions of the hemispheres are as follows:

$$\text{Hemisphere} = \begin{cases} \text{Jet}, & \Delta\Phi\left(1^\text{st}\,\text{jet}, 2^\text{nd}\,\text{jet}\right) < \Delta\Phi\left(\gamma, 2^\text{nd}\,\text{jet}\right), \\ \text{Photon}, & \text{else.} \end{cases} \tag{4.2}$$

The two response distributions coming from the different event topologies are separately evaluated. First, the resolution is determined for each of the configurations (cf. Fig. 4.4), and then, the weighted mean of the two contributions is calculated.

As can be seen in Fig. 4.4, events containing a second jet in the leading jet hemisphere lead to a response histogram with mean smaller one, while events with a second jet in photon direction result in a distribution with mean larger one. The former occurs more frequently because it contains jets from final and initial state radiation, while the latter mainly consists only from initial state radiation.

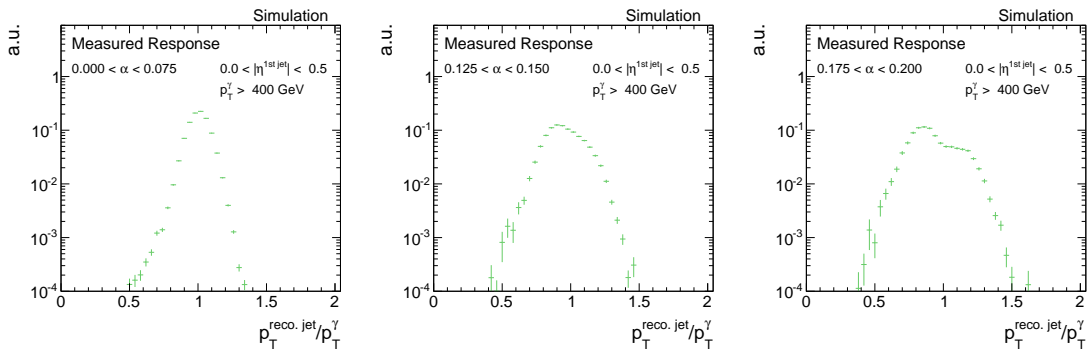The intrinsic part of the resolution for a given photon p_T bin is independent of secondary

Figure 4.2: The measured response $p_\mathrm{T}^\text{reco.\,jet}/p_\mathrm{T}^\gamma$ in simulation for FIXME : $p_\mathrm{T}^\gamma < 400\,\mathrm{GeV}$ for three different α ranges: $0.0 - 7.5\%$ (left), $12.5 - 15.0\%$ (middle) and $17.5 - 20.0\%$ (right). It can be seen that the double peak structure gets less pronounced for low α values.
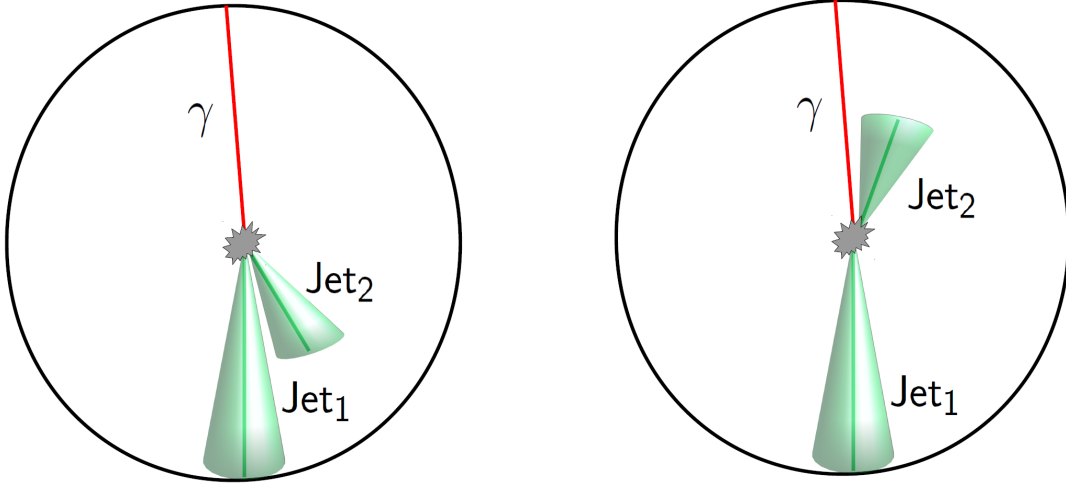
Figure 4.3: A schematic sketch of the two different event topologies where the second jet is in the leading jet (left) or the photon hemisphere (right)

jet p_T and thus can be considered as constant in terms of α

$$\sigma_{\mathrm{intrinsic}}\left(\alpha\right) = c. \tag{4.3}$$
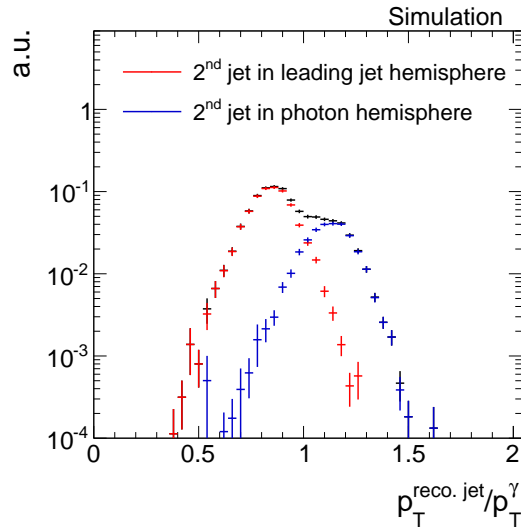

Figure 4.4: The measured response with the two contributions visualised. Events with a second jet in photon hemisphere (red) lead to a mean response larger one, while events with a second jet in the leading jet hemisphere (green) have a mean smaller one.

This is not true for the imbalance part. It was found empirically that the α dependence of the imbalance can be described by a linear function

$$\sigma_{\text{imbalance}}\left(\alpha\right) = q + m \cdot \alpha \tag{4.4}$$

Folding two independent Gaussian functions results in a quadratic addition of the corresponding standard deviations $\sigma_{\text{intr.}} \oplus \sigma_{\text{imb.}}$.

$$\sigma_{\text{total}}\left(\alpha\right) = \sqrt{c^2 + q^2 + 2\,q\,m \cdot \alpha + m^2 \cdot \alpha^2}. \tag{4.5}$$

In Fig. 4.5, the α dependence of the imbalance, the intrinsic resolution, and the total resolution is shown for two exemplary p_{T}^{γ} regions in simulated events. The measured intrinsic resolution and imbalance for various α values are fitted with functions (4.3) and (4.4), respectively. The measured total resolution (black dots) is fitted with function (4.5). Here, only c and m are free parameters, whereas q is fixed to the value obtained from the imbalance fit. All contributions are well described by their fit functions. The grey line is the total resolution with the analytic expression of function (4.5) with the parameters set to the fit values of the intrinsic and the imbalance fit.

It is apparent that the imbalance is not zero for $\alpha = 0$. This has two reasons. First and most important, only the photon and the parton are balanced in the transverse plane. But since the transverse momentum of a jet is defined as the sum of all particles' transverse
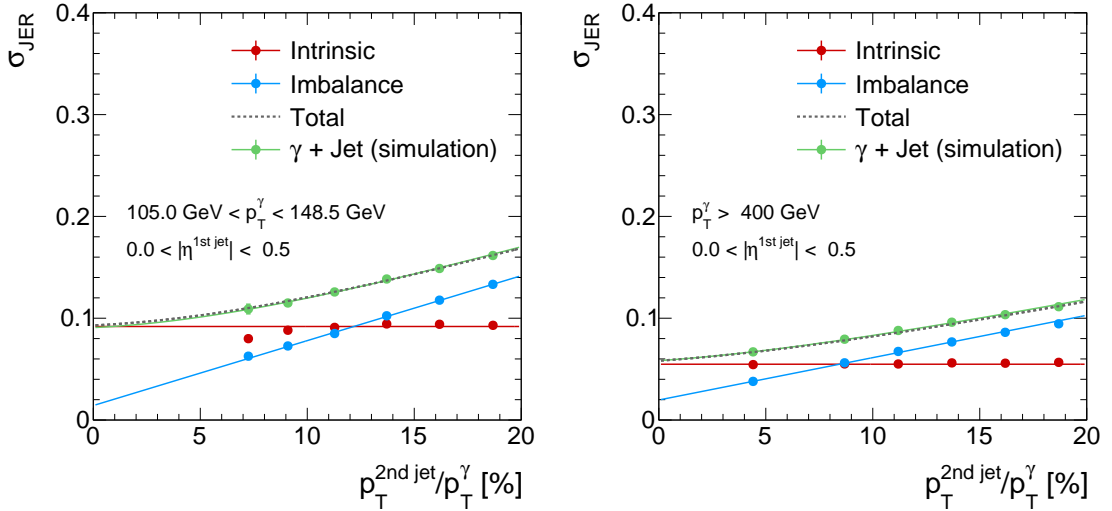

Figure 4.5: The alpha dependency of the various parts of the resolution in the simulated events for $83\,\text{GeV} < p_{\text{T}}^{\gamma} < 99\,\text{GeV}$ (left) and $400\,\text{GeV} < p_{\text{T}}^{\gamma}$ (right). The total resolution (grey dotted line) is the addition in quadrature of the imbalance (blue line) and the intrinsic (red line) fit functions. It can be compared to the measured pseudo data (green dots/line).

momenta that are clustered into the jet cone, the jet p_T can be lower than the p_T of the original parton. This effect is called out-of-cone showering and leads to a residual imbalance between the photon p_T and the generator-level jet p_T at $\alpha = 0$. Second, also the photon p_T can be wrongly measured and spoil the residual imbalance q.

These two effects lead to a small discrepancy between the measured resolution (black) and the intrinsic resolution (red) also for zero second jet p_T. To correct for this effect, q is fixed to the value obtained from fitting the imbalance part of the resolution (Eq. (4.4)) and then only the fit parameter c is taken as the relevant resolution from the fit. Also for measured data, q is fixed to the value obtained from simulation. Figure 4.6 shows the residual imbalance for two exemplary $|\eta^{\mathrm{1st\,jet}}|$ bins. It is almost stable and around 2% over the whole photon p_T range.

In Fig. 4.7, the fitted intrinsic resolution in simulation is shown in the different photon p_T bins for two different $|\eta^{\mathrm{1st\,jet}}|$ regions. The resolution improves for increasing photon p_T. For the $|\eta^{\mathrm{1st\,jet}}| < 0.5$ region, the resolution is approximately 10% for $p_T^\gamma \approx 100\,\mathrm{GeV}$ and decreases to values around 6% for $p_T^\gamma \approx 500\,\mathrm{GeV}$. The increasing statistical uncertainties for low photon p_T arise through the requirement of a maximal α and a minimal p_T of the second jet. This reduces the numbers of events in the low photon p_T bins. For events with $p_T^\gamma \lesssim 50\,\mathrm{GeV}$, it is not possible at all to fulfil both requirements at the same time.

The extrapolated intrinsic resolutions for the various photon p_T are fitted with the following function

$$\sigma_{\mathrm{JER}} = \sqrt{\mathrm{sgn(N)} \cdot \frac{\mathrm{N}}{p_T} + \mathrm{S}^2 \cdot p_T^{\mathrm{M}-1} + \mathrm{C}^2} \qquad (4.6)$$

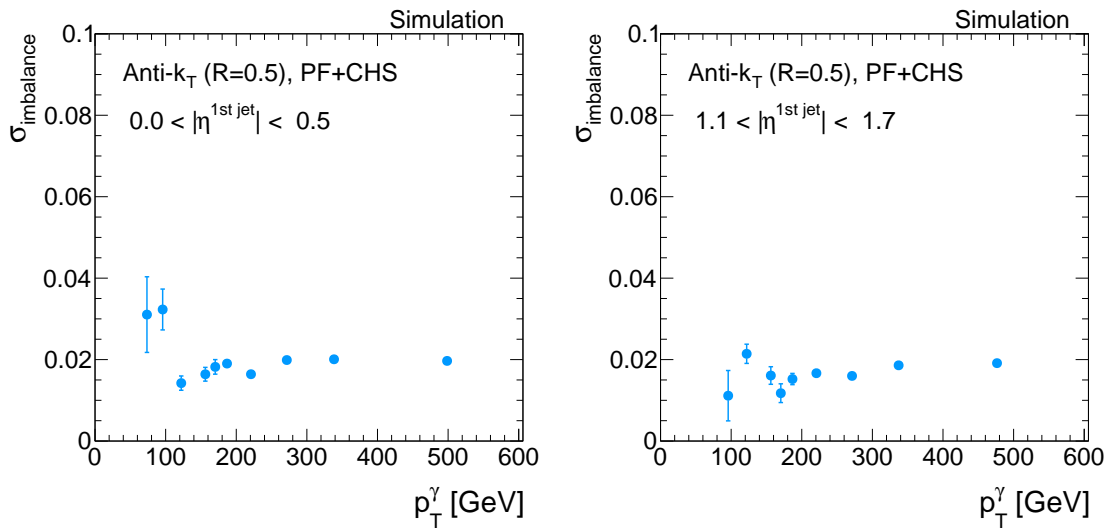which was introduced for particle flow jets in [6]. It is an extended fit function compared

Figure 4.6: Imbalance for $|\eta^{\mathrm{1st\,jet}}| < 0.5$ (left) and $1.1 < |\eta^{\mathrm{1st\,jet}}| < 1.7$ (right) in simulation.
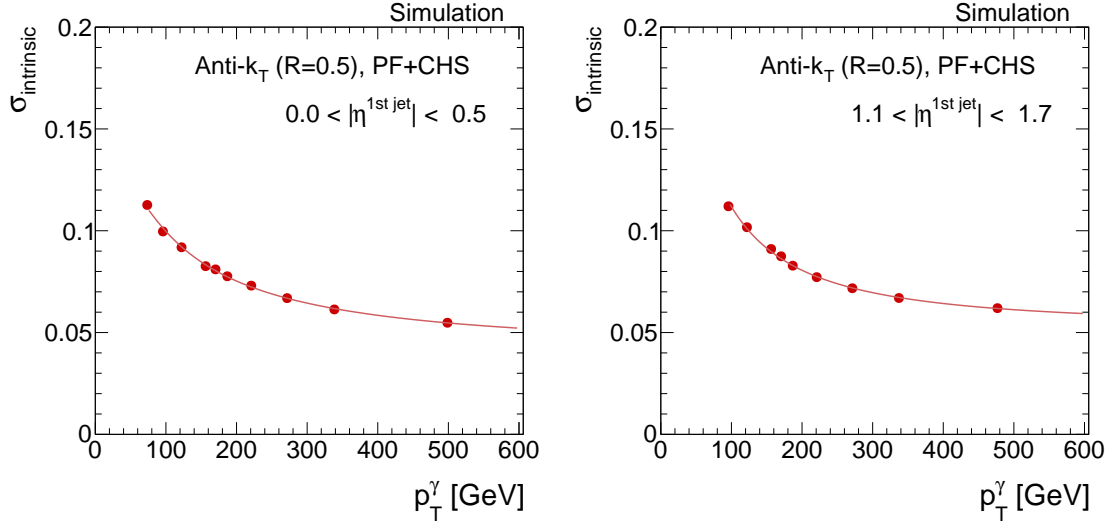
Figure 4.7: Intrinsic resolution for $|\eta^{1\text{st jet}}| < 0.5$ (left) and $1.1 < |\eta^{1\text{st jet}}| < 1.7$ (right) in simulation.

to the usual calorimeter resolution parametrisation to account for the higher resolution due to tracking information.

Finally, in order to measure data-to-simulation scale factors ρ_{res} for the jet transverse-momentum resolution, the measured resolution in data is divided by the resolution in Monte Carlo simulation (MC)

$$\rho_{\text{res}} = \frac{\sigma_{\text{JER}}^{\text{data}}}{\sigma_{\text{JER}}^{\text{MC}}} \tag{4.7}$$

It was found empirically, that this ratio is independent of p_{T}^{γ}, and can be fitted with a constant. Thus, to account for differences in the data-to-simulation ratio for different pseudorapidity ranges of the jet, the measurement of the scale factors is only done in bins of $|\eta^{1\text{st jet}}|$.

How to adjust finally the jet transverse-momentum resolution in simulation to the measured resolution in data is well described in [14].

4.1 Validation of the method

The method is validated with simulated events. The bias of the method is shown in Fig. 4.8 for the barrel region. It is evaluated as the ratio of the predicted intrinsic resolution by fitting Eq. (4.5) with q fixed to the value obtained by Eq. (4.4) over the intrinsic resolution directly obtained from the intrinsic response distribution $p_{\text{T}}^{\text{reco. jet}}/p_{\text{T}}^{\text{gen. jet}}$. The result is in good agreement with the expectation to better than 5% above 100 GeV and better than 1% above 200 GeV. Only for small p_{T}, larger deviations are observed, which are
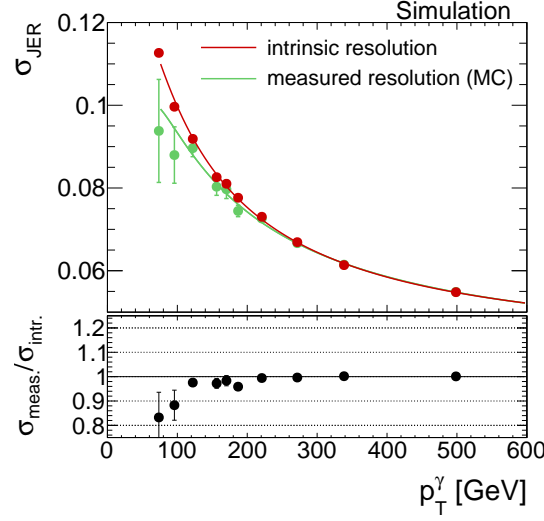
Figure 4.8: Consistency check of the method: Comparison between the "measured" resolution evaluated with Eq. (4.5) and the intrinsic resolution from Eq. (4.3) in simulation.

systematically lower than zero (up to 15%).

The residual bias of the method for small p_T^γ is stemming from two effects: First, the binning in p_T^γ and the momentum balance between the photon and the first two jets lead to a dependency of the first jet p_T on the second jet p_T and therefore alpha: For a fixed p_T^γ, the p_T of the first jet gets smaller for larger $p_T^{2^{nd}\,jet}$ in events where the second jet is in the leading jet hemisphere (see Fig. 4.3), leading to a dependency of $p_T^{1^{st}\,jet} \propto -p_T^{2^{nd}\,jet}$. This effect is directly opposite for events with a second jet in the photon hemisphere. In these events, the first jet p_T gets larger for larger $p_T^{2^{nd}\,jet}$ and thus $p_T^{1^{st}\,jet} \propto p_T^{2^{nd}\,jet}$ for fixed p_T^γ. As the resolution of the jet improves with higher jet p_T (see Fig. 4.7), a dependency of the leading jet p_T on the second jet p_T directly leads to a dependency of the intrinsic resolution on the second jet p_T. In principle, as the effect is opposite for events in the different hemispheres, it should cancel out, when taking the weighted mean of the two hemisphere resolutions. But as the topology of a second jet in the leading jet hemisphere is much more frequent, a residual upward trend in the intrinsic resolution vs. α is conserved.

The second source of the residual bias arises from the alpha definition $\alpha = p_T^{2^{nd}\,jet}/p_T^\gamma$. Because of the inclusion of p_T^γ in α with $\alpha \propto 1/p_T^\gamma$, the high photon p_T events accumulate in the low alpha regions. As the selected events are almost balanced, a high p_T^γ is associated with a high jet p_T, thus also the high jet p_T events accumulate in the low alpha bins, leading to an upward trend in the intrinsic resolution vs. α. This behaviour can be seen in the intrinsic resolution in Fig. 4.5, where a small increase of the resolution to high α can be seen. By fitting a horizontal line to the intrinsic resolution, this effect is

averaged out. But the measured resolution with an additional free parameter can adopt this increase and result, therefore, in a y-intercept which is too small. For high photon p_{T} bins, this effect is less pronounced, as the slope of $\mathrm{JER}(p_{\mathrm{T}}^{\gamma})$ (see Fig. 4.5) flattens out.

However, this is not of concern here, because the results of the measurement will be presented as resolution scale factors (ρ_{res}), defined as the resolution measured in data divided by the resolution measured in Monte Carlo simulation (see Eq. (4.7)). Hence, a possible bias in the separate resolution measurements for data and simulation should cancel out. To prove this hypothesis, the simulated dataset is smeared with input values $\rho_{\mathrm{res}} = 1.1$ in all $|\eta^{1^{\mathrm{st}}\,\mathrm{jet}}|$ bins. As done to determine the data-to-simulation ratio, the relative difference of the resolution measured in the smeared and in the non-smeared dataset is fitted with a constant over the photon p_{T} range. The resulting scale factors ρ_{res} should reproduce the input value of $\rho_{\mathrm{res}} = 1.1$.

In Fig. 4.9, the comparison of the input and output values is shown. In all $|\eta^{1^{\mathrm{st}}\,\mathrm{jet}}|$ bins, the measurement of the scale factors reproduces the input factors within the statistical uncertainties. The deviation of the measured scale factors to the input value is less than 0.9% in all four $|\eta^{1^{\mathrm{st}}\,\mathrm{jet}}|$ bins. Thus, the method is expected to hold also for the determination of the data-to-simulation ratio.

After the characterisation and estimation of the associated systematic uncertainties of the jet transverse-momentum resolution measurement with $\gamma + \mathrm{jet}$ events, the results of the measurement on $\sqrt{s} = 8\,\mathrm{TeV}$ data will be presented.
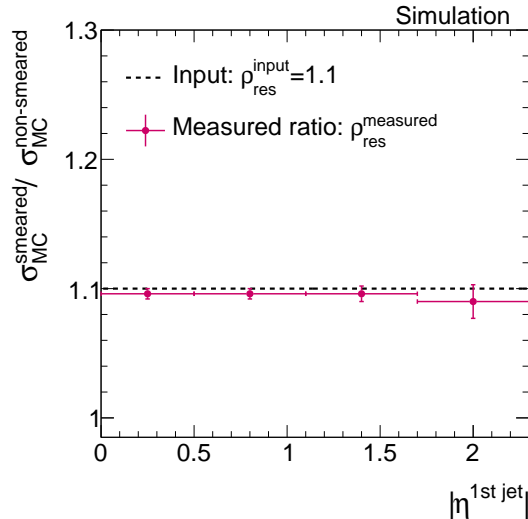

Figure 4.9: Comparison of the resolution ratio $\sigma_{\mathrm{JER}}^{\mathrm{smeared\ MC}}/\sigma_{\mathrm{JER}}^{\mathrm{non\text{-}smeared\ MC}}$ measured in simulated events with the input smearing factor $\rho_{\mathrm{res}} = 1.1$ in all four $|\eta^{1^{\mathrm{st}}\,\mathrm{jet}}|$ bins.

5 Systematic uncertainties

Many systematic uncertainties of the jet transverse-momentum resolution measurement cancel out when focusing on the data-to-simulation ratio $\sigma_{\text{JER}}^{\text{data}}/\sigma_{\text{JER}}^{\text{MC}}$. In the following subsections, only uncertainties relevant for this ratio will be discussed.

For the final uncertainty, the single uncertainties are added in quadrature, resulting in relative uncertainties between 2.3% to 6.3% for the lowest and highest $|\eta^{\text{1st jet}}|$ bin, respectively.

An overview of all systematic uncertainties can be found in Table 5.1.

Table 5.1: All relative systematic uncertainties on the data-to-simulation ratio $\sigma_{\text{JER}}^{\text{data}}/\sigma_{\text{JER}}^{\text{MC}}$ listed by sources for the different $|\eta^{\text{jet}}|$ bins.

	$|\eta^{\text{jet}}|$			
	0.0 - 0.5	0.5 - 1.1	1.1 - 1.7	1.7 - 2.3
Multijet contamination	+2.0%	+2.0%	+2.3%	+2.5%
	−2.0%	−2.0%	−2.3%	−2.5%
Simulation of flavor composition	+0.9%	+0.9%	+0.8%	+0.6%
	−0.9%	−0.9%	−0.8%	−0.6%
Simulation of out-of-cone showering	+0.5%	+2.8%	+3.6%	+5.7%
	−0.5%	−2.8%	−3.6%	−5.7%
Jet energy scale	+0.6%	+0.6%	+0.6%	+0.7%
	−0.5%	−0.6%	−0.6%	−0.6%
Pileup reweighting	+0.1%	+0.1%	+0.1%	+0.2%
	−0.1%	−0.1%	−0.2%	−0.2%
Total	+2.3%	+3.6%	+4.4%	+6.3%
	−2.3%	−3.6%	−4.4%	−6.3%

Uncertainty on the contamination with QCD-multijet events

Although the photon selection is very strict (see Section 3.3), due to the huge QCD-multijet cross section, a countable fraction of dijet events can survive the selection with a jet misidentified as photon. This happens, when e. g. a jet hadronises to a π^0 that decays to two photons which is sometimes not distinguishable from the isolated photon of a γ+jet event for the detector.

In principle, those dijet events have the same topology as γ+jet events. The two leading jets are also balanced apart from initial and final state radiation. Therefore, the method is generally expected to hold. A worsening of the resolution because of background contamination is only expected due to the mismeasurement of the p_T of the jet misidentified as photon, because only the energy of the π^0 is counted and not the full energy. Another aspect is the different flavor composition of a QCD-multijet sample. Due to the different production mechanism, QCD-dijets are predominantly initiated by gluons while the leading jet in γ + jet events often stems from a light quark, cf. Fig. 2.2. The number of particles after hadronisation is typically larger for gluon jets, hence the single particles are less energetic and out-of-cone showering is more pronounced. Since in this analysis the residual imbalance q is taken from the simulation where only a γ+jet sample is considered, it is not expected to accurately describe the residual imbalance in the data sample where also dijet events occur.

To investigate the impact of QCD-multijet contamination, a QCD-multijet sample, enriched in jets with a large electromagnetic fraction, is added to the γ + jet sample and weighted according to the cross section. Since the QCD-multijet sample has very large event weights leading to high statistical uncertainties in the measured jet transverse-momentum resolution, some selection criteria ($\alpha < 0.4$ and $\Delta\Phi > 2.7$) are relaxed in order to increase the statistical precision of the uncertainty estimation. Additionally, a rougher binning in α, p_T^γ and $|\eta^{1^\mathrm{st}\,\mathrm{jet}}|$ is applied.

The residual imbalance q of the resolution measurement including the QCD-multijet sample is fixed to the residual imbalance determined from the γ + jet only analysis to account for a possible error in the evaluation of the $\sigma_\mathrm{JER}^\mathrm{data}/\sigma_\mathrm{JER}^\mathrm{MC}$ ratio where data is only compared to a γ + jet sample.

In Fig. 5.1, the resolution measured when using both the γ + jet and the QCD-multijet sample is compared to the resolution measured only with the γ+jet sample. It can be seen, that the resolution is worse for low p_T^γ when considering QCD-multijet contamination.

The impact on the data-to-simulation ratio is estimated by adding the QCD-multijet sample on top of the γ + jet sample and redoing the evaluation of the scale factors. The resulting uncertainties vary between $2.0 - 2.5\%$ for the different $|\eta^{1^\mathrm{st}\,\mathrm{jet}}|$ regions (cf. Table 5.1).
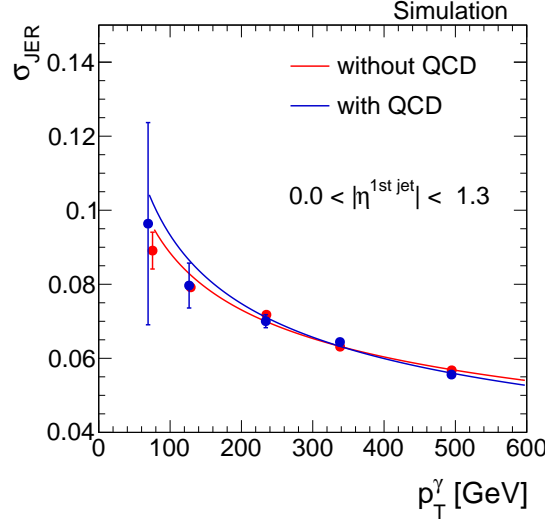
Figure 5.1: The jet transverse-momentum resolution measured in simulation for $|\eta^{1\text{st jet}}| <$ 1.3 with (blue) and without (green) a QCD-multijet sample added to the γ+jet sample.

Uncertainty on the flavor composition in simulation

A possible difference among the resolution of different jet flavors (caused by e.g. more pronounced out-of-cone showering of gluon jets) should in principle not play a role for the data-to-simulation scale factors ρ_{res} as long as the flavor composition of the data and simulation samples is the same.

To account for possible discrepancies in the flavor composition between data and simulation, the gluon and quark flavor fractions of the simulated sample are varied by 10%.

To estimate the effect of different flavour compositions, the resolution in simulation is separately evaluated for quarks ($\sigma_{\text{JER}}^{\text{quarks}}$) and gluons ($\sigma_{\text{JER}}^{\text{gluons}}$). There are various definitions used in the CMS collaboration how to assign the underlying generator-level quark/gluon flavor to a jet. In this measurement the so-called "algorithmic" flavor definition is used which classifies b- or c-jets from gluon splitting as b- or c-quarks (see Appendix A.3 for more details on this definition).

Figure 5.3 shows the differences in the resolution for all flavors separately for $|\eta^{1\text{st jet}}| <$ 1.3. The composition in the simulated PYTHIA γ + jet sample is around 60% light quarks and 20% to 35% gluons (see Fig. 5.2). The missing fraction is mainly made up out of charm quarks.

The resolution for gluon and light quark jets is comparable for small p_{T}^{γ} and gets larger for high p_{T}^{γ}. Since the transverse momentum of neutrinos is counted into the generator-level jet p_{T}, the resolution of charm and bottom quarks is therefore shifted to larger resolution values (left part of Fig. 5.3). This is not the case, if the neutrino p_{T} is not
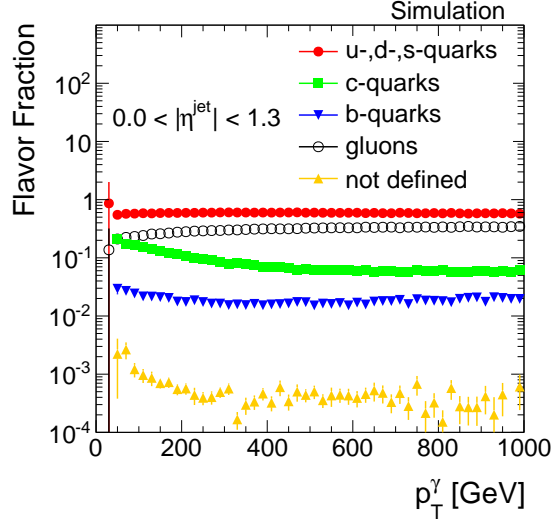
Figure 5.2: The flavor composition in the γ+jet sample in the barrel region of the detector. The "algorithmic" flavor definition is used (see Appendix A.3 for more details).

added to the generator-level jet p_T, as can be seen in Fig 5.3 (right). However, for the here presented measurement is does not play a role whether the neutrino p_T is or is not added to the generator-level jet p_T, because in case it is not included into the intrinsic response the long right tail of the response function for b- and c-quarks is then transferred to the imbalance response. Thus, the right tail of b- and c-quarks does anyway enter
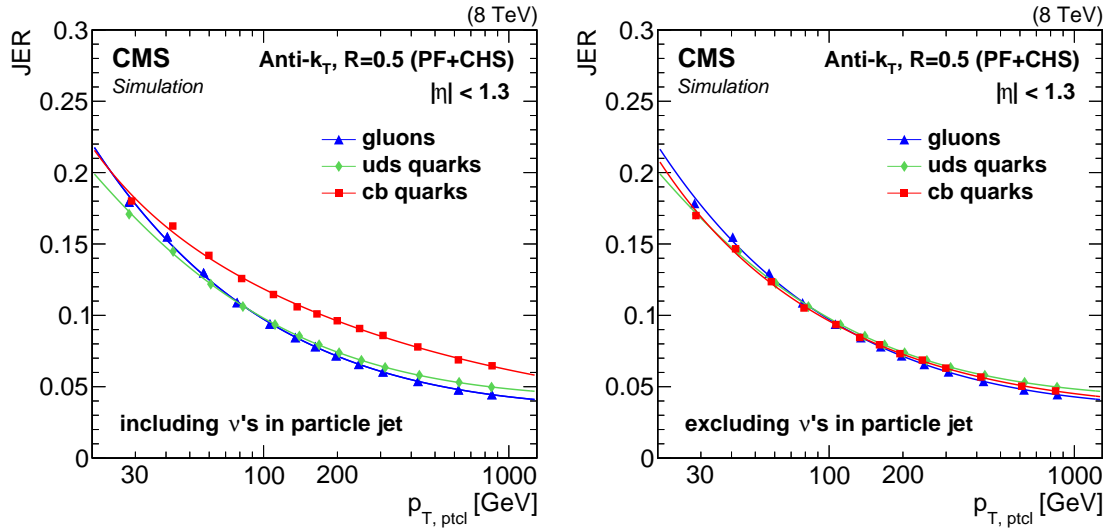

Figure 5.3: The intrinsic resolution $\sigma_{intr.}$ for $|\eta^{1^{st}\,jet}| < 1.3$ for different jet flavors with (left) and without (right) including the neutrinos in the generator-level jet. Here, JER refers to $\sigma_{intr.}$, and $p_{T,\,ptcl}$ to the generator-level jet p_T.

the jet transverse-momentum resolution measurement with $\gamma + \text{jet}$ events, either in the intrinsic or in the imbalance response.

The weighted mean of the quark and the gluon resolution is then taken to estimate the resolution for different flavor compositions, such that the flavor fractions are varied by 10%. Finally, the constant fit to the data-to-simulation ratio $\sigma_{\text{JER}}^{\text{data}}/\sigma_{\text{JER}}^{\text{MC}}$ is reevaluated, leading to a final systematic uncertainty between $0.6 - 0.9\%$.

Uncertainty on the simulation of out-of-cone showering

Another source of uncertainty is the use of information from Monte Carlo simulation by determining the residual imbalance q from the simulated $\gamma + \text{jet}$ sample (Eq. (4.5)).

Since it cannot be expected that out-of-cone showering is well modelled in simulation, possible differences between real and simulated out-of-cone showering are estimated by the evaluation of the ratio $\sigma_{\text{JER}}^{\text{data}}/\sigma_{\text{JER}}^{\text{MC}}$ using different jet radii of the jet reconstruction algorithm.

For the primary analysis, jets reconstructed by the Anti-k_t algorithm with a radius of $R = 0.5$ are used (AK5-jets). In order to evaluate the systematic uncertainty on the out-of-cone showering simulation, the measurement of ρ_{res} redone with jets reconstructed with a jet radius of $R = 0.7$ (AK7-jets).

The data-to-simulation ratio is in all $|\eta^{1^{\text{st}}\,\text{jet}}|$ bins larger for AK7-jets, resulting in uncertainties between $0.5 - 5.7\%$. The uncertainty on the simulation of out-of-cone showering is thereby the largest systematic uncertainty of this measurement.

Uncertainty on the jet energy scale

A further uncertainty arises from the correction of the jet energy scale. The transverse momentum of each jet is corrected in order to have uniform response over the full η^{jet}, and $p_{\text{T}}^{\text{jet}}$ range [15]. In simulation, it is additionally corrected to account for data-simulation differences. The latter correction can be a important for the evaluation of the data-to-simulation ratio ρ_{res}. Thus, the uncertainties on the correction factors that are only applied to the simulated samples are varied up and down within their 1σ-uncertainties.

The effect of the jet p_{T} variation on the data-to-simulation ratio is of minor importance and range between $0.5 - 0.7\%$.

Uncertainty on the pileup reweighting

Finally, an uncertainty due to the adjustment of the simulated events to the pileup distribution in data is evaluated.

To account for this uncertainty, the effect of a 5.0% up- and downward variation of the minimum-bias cross section (69.4 mb) on the resolution is evaluated, following the recommended procedure from [16]. The resulting uncertainties are almost negligible and range between $0.1 - 0.2\%$.

6 Results

The data-to-simulation resolution scale factors ρ_{res} are determined in $19.7\,\text{fb}^{-1}$ of pp-collision data at $\sqrt{s} = 8\,\text{TeV}$ with the methodology described in Chapter 4. In each α-, p_{T}^{γ}- and $|\eta^{\text{1st jet}}|$-bin, the width of the 99% truncated response histogram is determined in simulation and data. Afterwards, the extrapolation to zero additional jet activity is carried out, by fixing the imbalance q in simulation and in data to the value extracted from the imbalance extrapolation in simulation. Exemplary extrapolations for the imbalance and the total resolution in data and simulation are shown in Fig. 6.1.

The full set for each p_{T}^{γ} and $|\eta^{\text{1st jet}}|$ bin can be found in Appendix A.4.
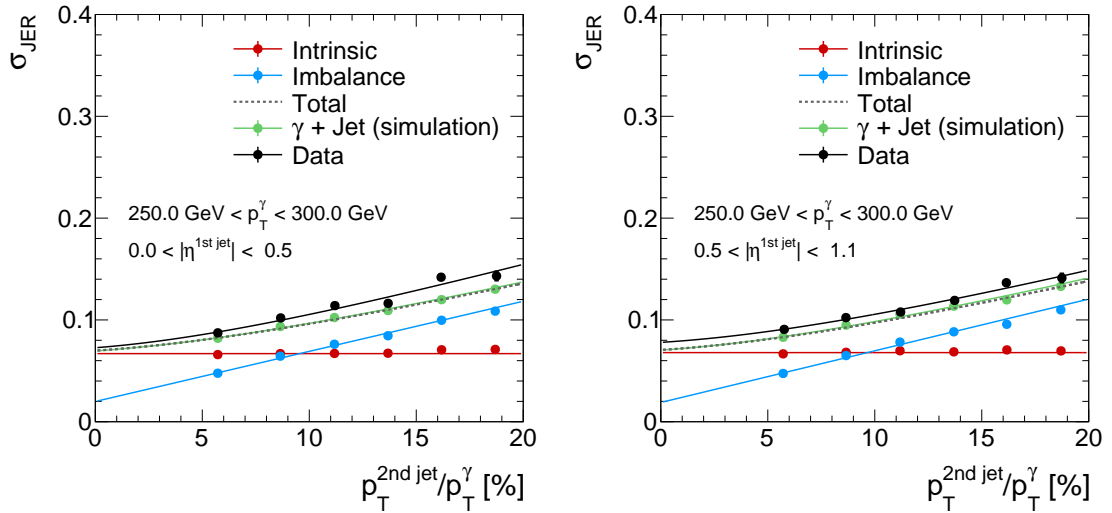

Figure 6.1: Two examples of the alpha dependency of the measured jet transverse-momentum resolution in data (black dots), in simulation (green dots) and of the intrinsic (red dots) and the imbalance (blue dots) part of the resolution in simulated events. All resolutions are fitted with the corresponding functions introduced in Chapter 4 (Eqs. (4.3)- (4.5)). The total resolution (grey dotted line) is the addition in quadrature of the imbalance (blue line) and the intrinsic (red line) fit functions.

Finally, the extracted resolutions in data and simulation in every p_T^γ bin are divided and a horizontal fit is applied to this ratio

$$\frac{\sigma_{\mathrm{JER}}^{\mathrm{data}}}{\sigma_{\mathrm{JER}}^{\mathrm{MC}}}\left(p_T^\gamma\right).$$

In Fig. 6.2, the results for all four $|\eta^{1^{\mathrm{st}}\,\mathrm{jet}}|$-ranges are depicted. The χ^2/NDF-values for the four fits vary between 0.23 and 2.53. Thus, a horizontal fit is justified, and one value for every $|\eta^{1^{\mathrm{st}}\,\mathrm{jet}}|$-bin will be reported.
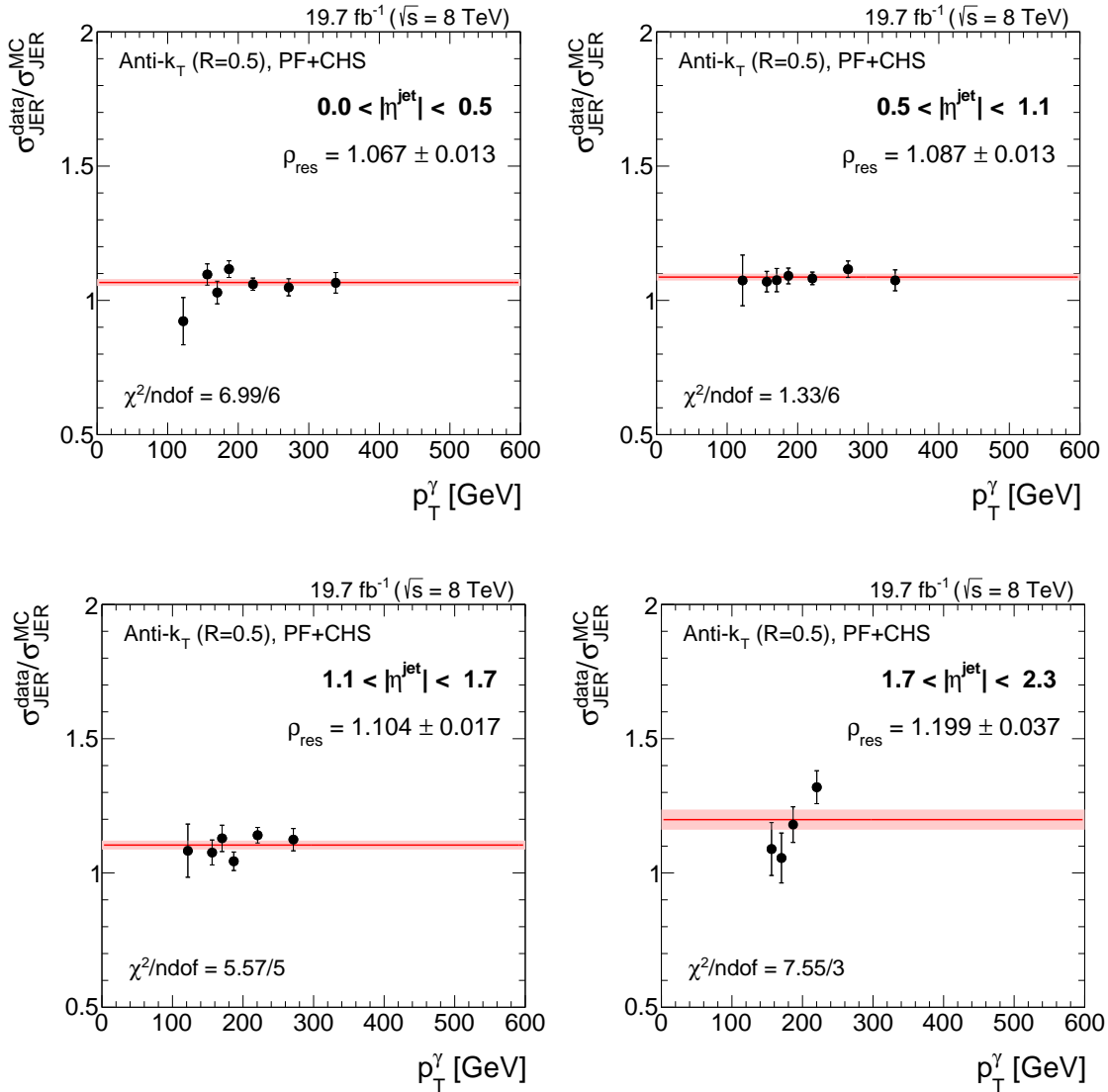

Figure 6.2: Data-to-simulation resolution ratios (black dots), fitted with a horizontal line (red line) for four different $|\eta^{\mathrm{jet}}|$-ranges. The fit uncertainties are depicted with light red error bands.

Table 6.1: Data-to-simulation resolution scale factors ρ_{res} with statistical and systematic uncertainties.

$|\eta^{\mathrm{jet}}|$	ρ_{res}	stat.	sys.
$0.0 - 0.5$	1.067	± 0.013	$^{+0.025}_{-0.024}$
$0.5 - 1.1$	1.087	± 0.013	$^{+0.039}_{-0.039}$
$1.1 - 1.7$	1.104	± 0.017	$^{+0.049}_{-0.049}$
$1.7 - 2.3$	1.199	± 0.037	$^{+0.075}_{-0.075}$

All fit results are greater than one which means that the resolution in data is in all bins worse compared to the resolution in simulation. The values of the fits range from 1.067 (for the first η^{jet}-bin) to 1.199 (for the last η^{jet}-bin).

The systematic uncertainties are evaluated as described in the previous chapter. The single uncertainties are taken as upper and lower boundary of the 68% uncertainty band and are added in quadrature to get the total systematic uncertainty. Table 6.1 summarises the data-to-simulation ratio results determined with data collected during the year 2012 with their statistical and systematic uncertainties. The visualised result can be found in Fig. 6.3.

Though the γ+jet analysis is known to be capable to produce highly precise results, the systematic uncertainties are still dominating. This is mainly caused by the uncertainty on the simulation of out-of-cone showering. The statistical limitation of this analysis is due to the collected data at the CMS detector. The number of simulated events is roughly eight times larger.

6.1 Comparison to 2011 measurement

A comparison of the data-to-simulation resolution scale factors ρ_{res} between this analysis and the results of 2011 which were determined from a dijet data sample [14] can be found in Fig. 6.4.

It can be seen, that throughout the whole η^{jet}-range the data-to-simulation are systematically larger for the result in 2011.

Comparing the precision of both measurements, the γ+jet analysis is for all η-bins more precise than the analysis done with dijet events. This is due to the smaller systematic
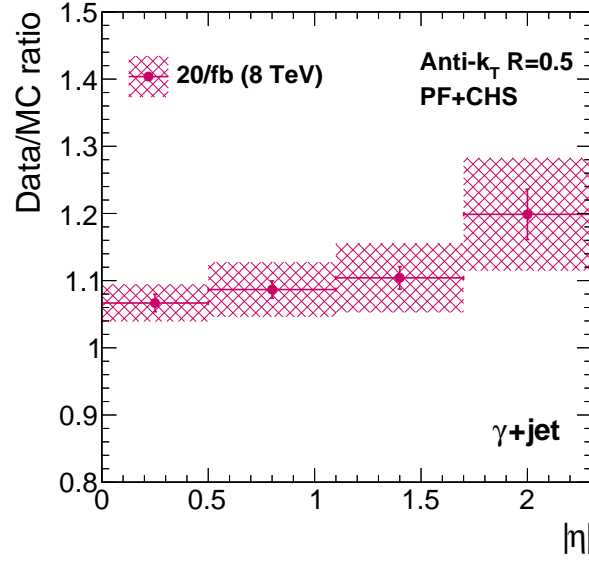
Figure 6.3: The measured data-to-simulation resolution ratio in $\gamma + \text{jet}$ events using data recorded in the year 2012. The red band depicts the total uncertainty whereas the error bars show the statistical uncertainty only.
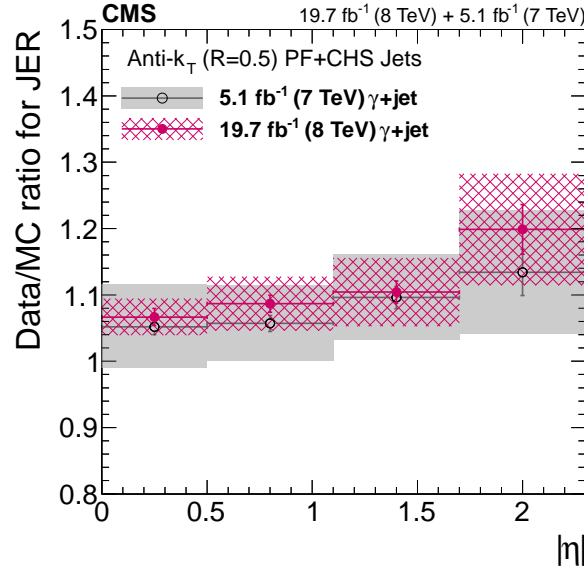

Figure 6.4: FIXME (update this plot): Data-to-simulation jet p_T resolution ratio determined from $\gamma + \text{jet}$ events from 2012 compared to dijet results from 2011. The grey and magenta bands correspond to the full uncertainties, whereas the error bars depict the statistical uncertainties only.

uncertainties of the $\gamma + \text{jet}$ analysis which compensates for the better statistical precision of the QCD-multijet sample due to the large cross section.

6.2 Comparison to 2012 dijet measurement

In 2012, also a jet p_T resolution measurement was conducted with the help of dijet events [15, 17]. A comparison of the here presented measurement using $\gamma + \text{jet}$ events to the measurement with dijet events can be found in Fig. 6.5. Both measurements are compatible within their uncertainties. It can be seen that the statistical precision is much better for the measurement with QCD-multijet events because of the larger cross section. The systematic uncertainties are of comparable size for small pseudorapidity bins and are larger for high $|\eta^{\text{jet}}|$ in the $\gamma + \text{jet}$ measurement. This is due to the uncertainty on the simulation of the out-of-cone showering. This uncertainty plays a smaller role in the dijet measurement (between 0.4% and 1.5%) as the effect by out-of-cone showering partly cancels out in case of two balanced jets.
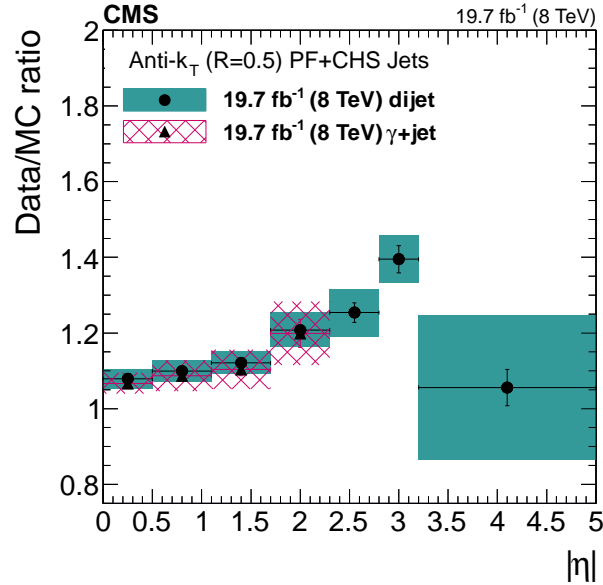

Figure 6.5: FIXME: Data-to-simulation jet p_T resolution ratio determined from $\gamma + \text{jet}$ events from 2012 compared to dijet results from 2012. The blue and magenta bands correspond to the full uncertainties, whereas the error bars depict the statistical uncertainties only.

7 Discussion and conclusion

The difference between data and simulation of the jet-transverse momentum resolution is an important input for many analyses at CMS, among them searches for physics beyond the Standard Model using QCD-multijet events, e. g. [3].

In the here presented analysis, the first measurement of the data-to-simulation resolution ratio $\sigma_{\mathrm{JER}}^{\mathrm{data}}/\sigma_{\mathrm{JER}}^{\mathrm{MC}}$ using $\gamma+\mathrm{jet}$ events with $19.7\,\mathrm{fb}^{-1}$ pp-collision data at $\sqrt{s}=8\,\mathrm{TeV}$ collected in 2012 at the CMS detector was carried out. For this purpose, the methodology introduced in [6, 7] was further developed. To take account of the double peak structure when applying an exclusive binning in the variable α which measures the additional jet activity in the event, the event selection explicitly distinguishes the case of parton radiation in the leading jet/photon hemispheres. This change in methodology is introduced for the first time by this measurement.

The resolution in data is found to be systematically larger than in simulation throughout the investigated η^{jet} plane. A possible p_{T}^{γ} dependence of the resolution scale factors ρ_{res} is not visible. Thus, the ratio is parametrised with a constant per η^{jet}-bin.

The relative difference of the data resolution ranges from $\sim 7\%$ to $\sim 20\%$ for $|\eta^{\mathrm{jet}}|$ between $0.0-0.5$ and between $1.7-2.3$, respectively, with total statistical and systematic uncertainties between 3% and 8%.

The here presented measurement serves as a cross-check measurement to the jet p_{T} resolution ratio result using dijet events [15, 17]. Both measurements are compatible within their statistical and systematic uncertainties.

For a future measurement, a reduction of the uncertainties is desirable. Since the systematic uncertainty is still dominating, most notably the uncertainty on the simulation of out-of-cone showering, an improved evaluation of the out-of-cone showering uncertainty could significantly improve the precision of the data-to-simulation ratio $\sigma_{\mathrm{JER}}^{\mathrm{data}}/\sigma_{\mathrm{JER}}^{\mathrm{MC}}$. A better evaluation can be possibly achieved by a better understanding, whether the difference of ρ_{res} using clustered jets within a radius of 0.7 and 0.5 is only originating from out-of-cone showering effects. Since the simulation of out-of-cone showering should in principal only enter the result by the residual imbalance q, an overestimation by the here presented method might be possible.

Furthermore, an increase in the statistical precision is desirable to allow for the coverage of the measurement of the resolution scale factors in the high pseudorapidity regions which

has not been possible so far.

A Measurement of the jet transverse-momentum resolution
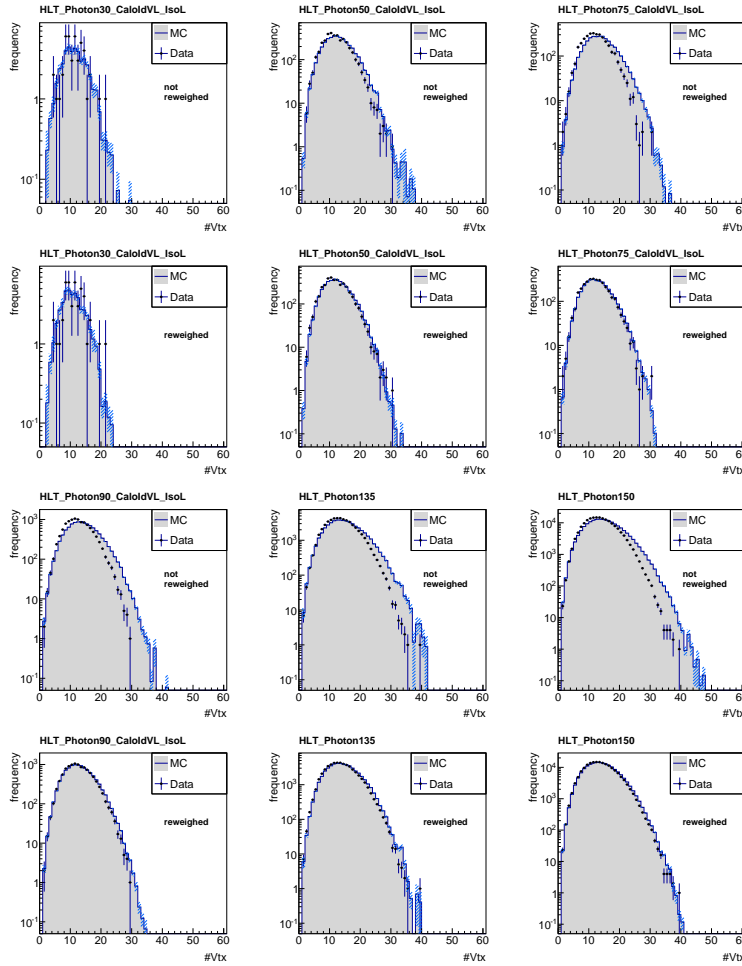
A.1 Pileup reweighting

Figure A.1: The number of primary vertices in data and simulation before (1st row) and after (2nd row) pileup reweighting for $36\,\mathrm{GeV} < p_\mathrm{T}^{\gamma} < 60\,\mathrm{GeV}$ (left), $60\,\mathrm{GeV} < p_\mathrm{T}^{\gamma} < 88\,\mathrm{GeV}$ (middle), and $88\,\mathrm{GeV} < p_\mathrm{T}^{\gamma} < 105\,\mathrm{GeV}$ (right) and the number of primary vertices in data and simulation before (3rd row) and after (4th row) pileup reweighting for $105\,\mathrm{GeV} < p_\mathrm{T}^{\gamma} < 149\,\mathrm{GeV}$ (left), $149\,\mathrm{GeV} < p_\mathrm{T}^{\gamma} < 165\,\mathrm{GeV}$ (middle), and $165\,\mathrm{GeV} < p_\mathrm{T}^{\gamma}$ (right).

A.2 Summary of all selection requirements

Table A.1: Summary of all selection criteria for the measurments of the jet transverse-momentum resolution with $\gamma + $ jet events.

One jet with	$p_\mathrm{T} > 10\,\mathrm{GeV}$
	Neutral hadron fraction < 0.90
	Neutral electromagnetic fraction < 0.90
	Number of constituents > 1
	Charged hadron fraction > 0
	Charged hadron multiplicity > 0
One photon with	$p_\mathrm{T} > 22\,\mathrm{GeV}$
	$|\eta| < 1.3$
	$\frac{\mathrm{H}}{\mathrm{E}} < 0.05$
	$\sigma_{i\eta i\eta} < 0.013$
	ECAL isolation $< 4.2\,\mathrm{GeV} + 0.0060 \cdot p_\mathrm{T}^{\gamma}$
	HCAL isolation $< 2.2\,\mathrm{GeV} + 0.0025 \cdot p_\mathrm{T}^{\gamma}$
	Track Isolation $< 2.0\,\mathrm{GeV} + 0.0010 \cdot p_\mathrm{T}^{\gamma}$
	Pixel seed veto
Event-based selection	$p_\mathrm{T}^{\mathrm{2nd\ jet}} > 10\,\mathrm{GeV}$
	$\frac{p_\mathrm{T}^{\mathrm{2nd\ jet}}}{p_\mathrm{T}^{\gamma}} < 0.20$
	$\Delta\Phi\left(1^{\mathrm{st}}\,\mathrm{jet},\,\gamma\right) > 2.95$

A.3 Generator-level jet flavor definition

The algorithmic flavor definition uses the following discrimination:

- Try to find the parton that most likely determines the properties of the jet and assign that flavor as true flavor

- Here, the "final state" partons (after showering, radiation) are analyzed (also within $\Delta R < 0.3$ of reconstructed jet cone)

- Jets from radiation are matched with full efficiency

- If there is a b/c within the jet cone: label as b/c

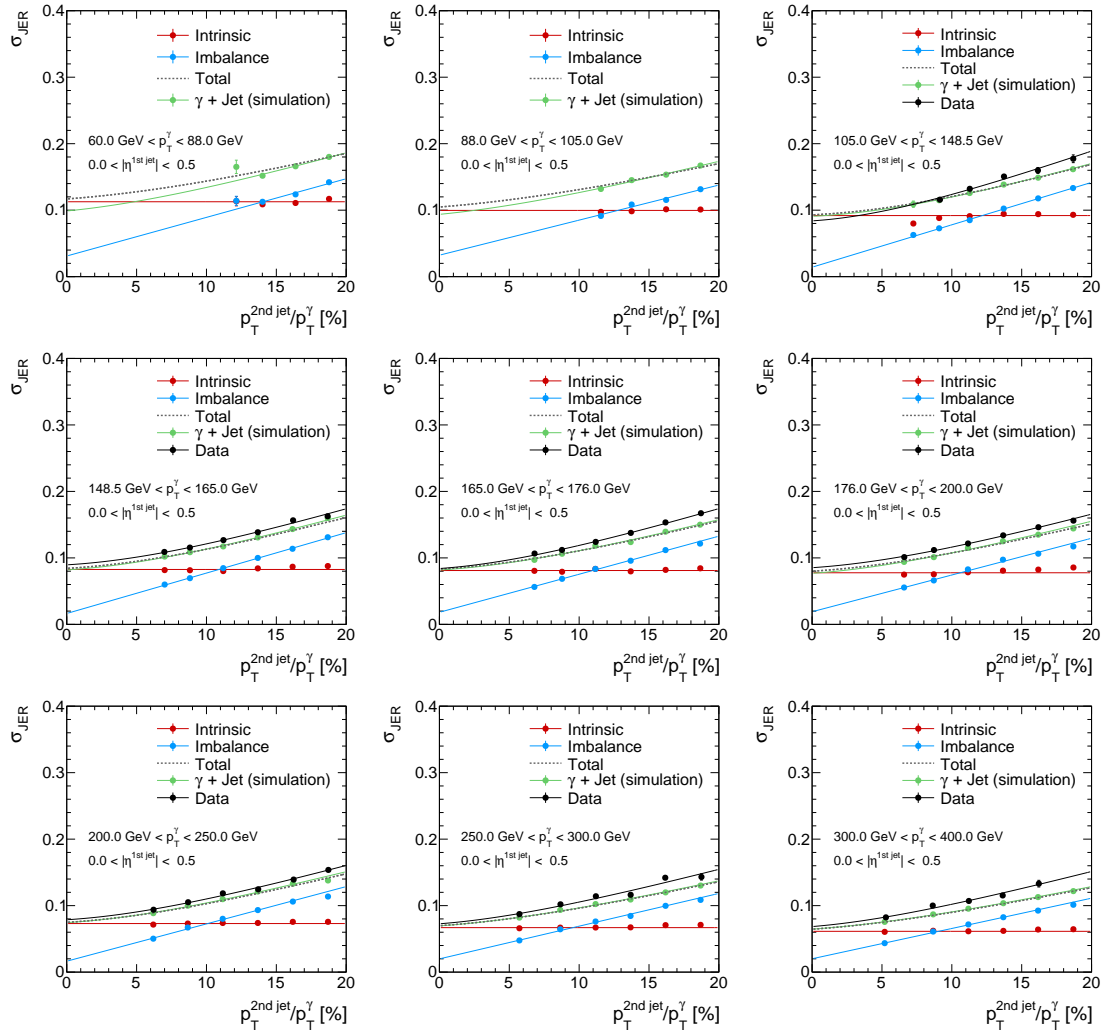- Otherwise: assign flavor of the hardest parton

A.4 Extrapolation plots

Figure A.2: $\sigma_{\mathrm{JER}}(\alpha)$ of the intrinsic, imbalance and total resolution in simulation and the resolution measured in data for all $|\eta^{1\mathrm{st\,jet}}|$ and p_{T}^{γ} bins.
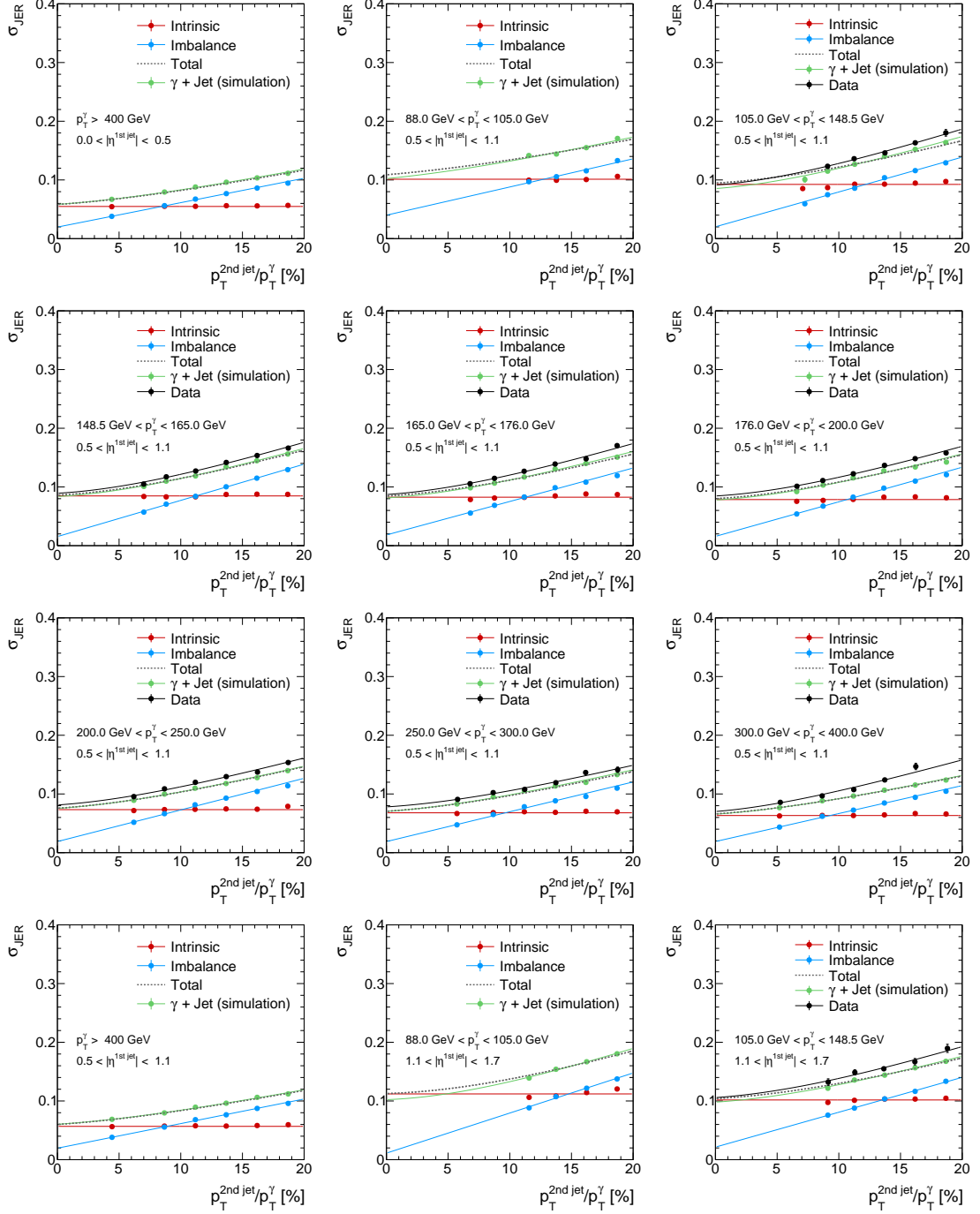
Figure A.3: Continued from Fig. A.2: σ_{JER} (α) of the intrinsic, imbalance and total resolution in simulation and the resolution measured in data for all $|\eta^{1^{\mathrm{st}}\,\mathrm{jet}}|$ and p_{T}^{γ} bins.
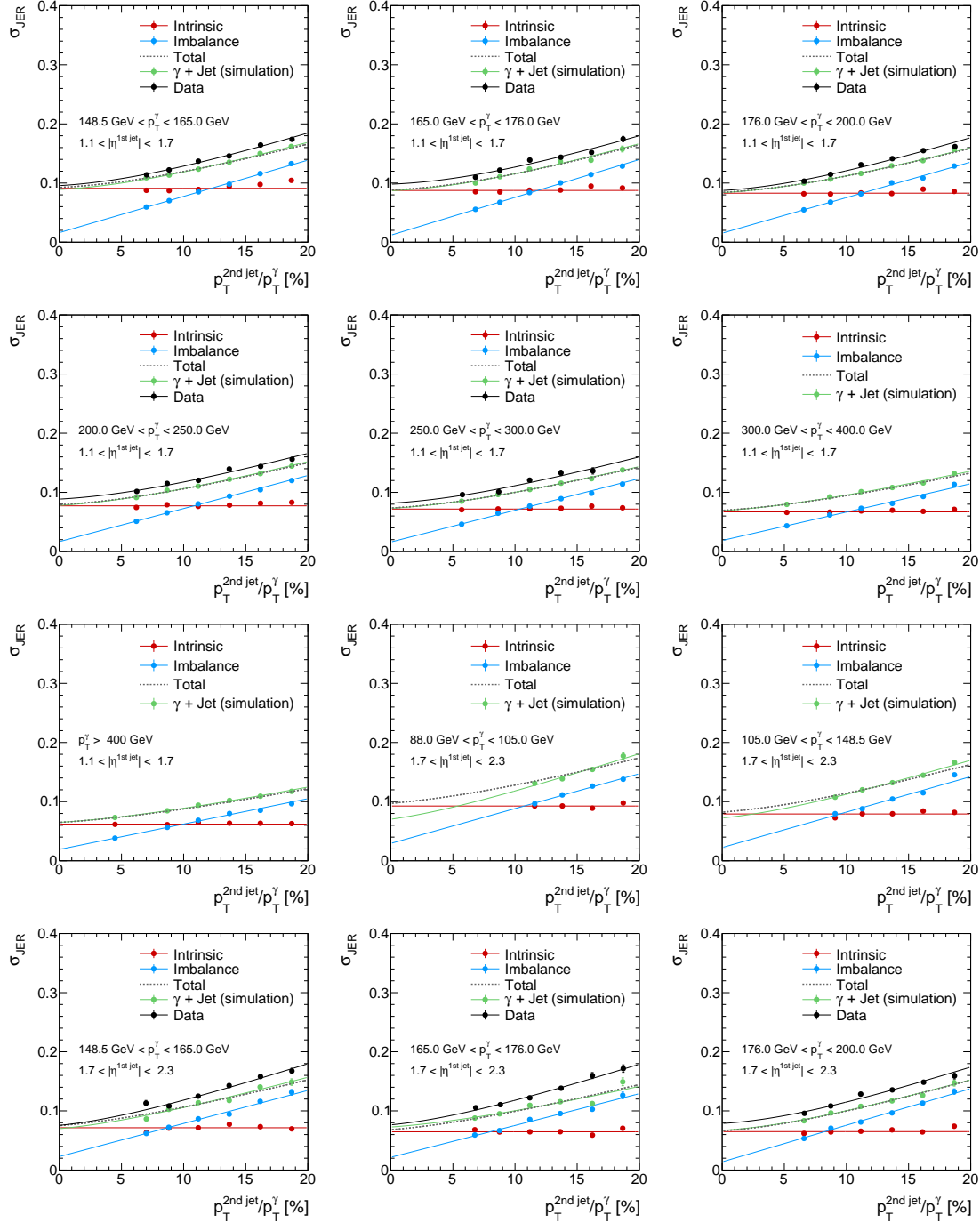
Figure A.4: Continued from Fig. A.3: σ_{JER} (α) of the intrinsic, imbalance and total resolution in simulation and the resolution measured in data for all $|\eta^{\mathrm{1st\,jet}}|$ and p_{T}^{γ} bins.
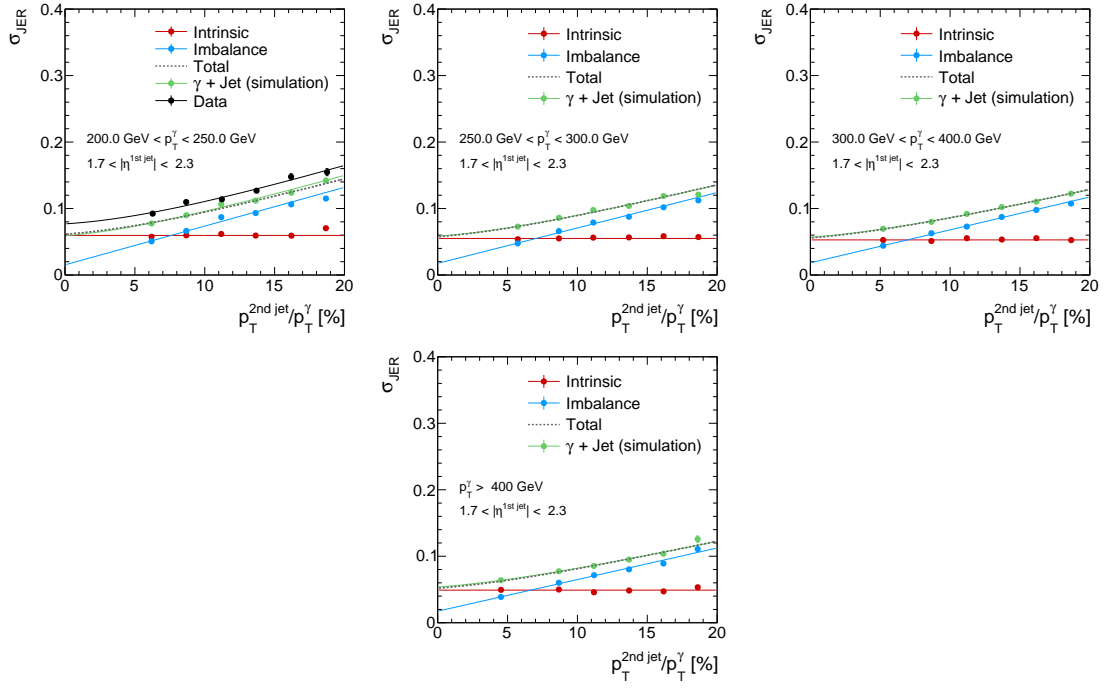
Figure A.5: Continued from Fig. A.4: σ_{JER} (α) of the intrinsic, imbalance and total resolution in simulation and the resolution measured in data for all $|\eta^{1\mathrm{st\,jet}}|$ and p_{T}^{γ} bins.

Bibliography

[1] CMS Collaboration, "Measurements of differential dijet cross section in proton-proton collisions at $\sqrt{(}s) = 8$ TeV with the CMS detector", *CMS Physics Analysis Summary* **CMS-PAS-SMP-14-002** (2014).

[2] CMS Collaboration, "Measurement of the differential cross section for top quark pair production in pp collisions at $\sqrt{s} = 8$ TeV", *Eur. Phys. J.* **C75** (2015), no. 11, 542, `arXiv:1505.04480`. `doi:10.1140/epjc/s10052-015-3709-x`.

[3] CMS Collaboration, "Search for new physics in the multijet and missing transverse momentum final state in proton-proton collisions at $\sqrt{s} = 8$ TeV", *JHEP* **06** (2014) 055, `arXiv:1402.4770`. `doi:10.1007/JHEP06(2014)055`.

[4] CMS Collaboration, "Searches for Supersymmetry using the M_{T2} Variable in Hadronic Events Produced in pp Collisions at 8 TeV", *JHEP* **05** (2015) 078, `arXiv:1502.04358`. `doi:10.1007/JHEP05(2015)078`.

[5] CMS Collaboration, "Search for supersymmetry in hadronic final states with missing transverse energy using the variables α_T and b-quark multiplicity in pp collisions at $\sqrt{s} = 8$ TeV", *Eur. Phys. J.* **C73** (2013), no. 9, 2568, `arXiv:1303.2985`. `doi:10.1140/epjc/s10052-013-2568-6`.

[6] CMS Collaboration, "Determination of Jet Energy Calibration and Transverse Momentum Resolution in CMS", *JINST* **6** (2011) P11002, `arXiv:1107.4277`. `doi:10.1088/1748-0221/6/11/P11002`.

[7] CMS Collaboration, "Jet Energy Resolution in CMS at sqrt(s)=7 TeV", *CMS Physics Analysis Summary* **CMS-PAS-JME-10-014** (2011).

[8] CMS Collaboration, "Performance of Photon Reconstruction and Identification with the CMS Detector in Proton-Proton Collisions at $\sqrt{s} = 8$ TeV", *JINST* **10** (2015), no. 08, P08010, `arXiv:1502.02702`. `doi:10.1088/1748-0221/10/08/P08010`.

[9] CMS Collaboration, "Particle-Flow Event Reconstruction in CMS and Performance for Jets, Taus, and MET", *CMS Physics Analysis Summary* **CMS-PAS-PFT-09-001** (2009).

[10] M. Cacciari, G. P. Salam, and G. Soyez, "The anti-k_t jet clustering algorithm",
     JHEP **04** (2008) 063, `arXiv:0802.1189`. `doi:10.1088/1126-6708/2008/04/063`.

[11] N. Odell, "PF Jet ID Recommendation".
     `https://indico.cern.ch/event/89919/contribution/0/attachments/1091238/`
     `1556772/PF_JET_ID_Reccomendation.pdf`, April, 2010.

[12] N. Saoulidou and E. Tziaferi, "Performance of the Particle-Flow jet identification
     criteria using proton-proton collisions at $\sqrt{s} = 8$ TeV", *CMS Analysis Note*
     CMS-AN-14-227 (2014). Internal documentation.

[13] CMS Collaboration, "Isolated Photon Reconstruction and Identification at
     $\sqrt{s} = 7$ TeV", *CMS Physics Analysis Summary* **CMS-PAS-EGM-10-006** (2011).

[14] M. Schröder, "Quality of jet measurements and impact on a search for new physics
     at CMS". PhD thesis, Hamburg U., 2012.
     `http://www-library.desy.de/cgi-bin/showprep.pl?thesis12-042`.

[15] CMS Collaboration, "Jet Energy Scale and Resolution in the CMS Experiment",
     CMS Physics Analysis Summary **CMS-PAS-JME-13-004** (2015).

[16] CMS Collaboration, "Pileup Reweighting", *Internal CMS Wiki* (2011).
     https://twiki.cern.ch/twiki/bin/viewauth/CMS/PileupReweighting.

[17] K. Goebel, "Probing supersymmetry based on precise jet measurements at the CMS
     experiment". PhD thesis, U. Hamburg, Dept. Phys., 2015.
     `http://www-library.desy.de/cgi-bin/showprep.pl?thesis15-003`.